Scanning ultrafast Sagnac interferometry for imaging two-dimensional surface wave propagation

Takehiro Tachizaki, Toshihiro Muroya, and Osamu Matsuda[a)]
Department of Applied Physics, Graduate School of Engineering, Hokkaido University, Sapporo 060-8628, Japan

Yoshihiro Sugawara
School of Physics and Astronomy, University of Southampton, Southampton SO17 1BJ, United Kingdom

David H. Hurley
Idaho National Laboratory, Idaho Falls, Idaho 83415-2209

Oliver B. Wright
Department of Applied Physics, Graduate School of Engineering, Hokkaido University, Sapporo 060-8628, Japan

(Received 10 February 2006; accepted 16 March 2006; published online 24 April 2006)

We describe an improved two-dimensional optical scanning technique combined with an ultrafast Sagnac interferometer for delayed-probe imaging of surface wave propagation. We demonstrate the operation of this system, which involves the use of a single focusing objective, by monitoring surface acoustic wave propagation on opaque substrates with picosecond temporal and micron lateral resolutions. An improvement in the lateral resolution by a factor of 3 is achieved in comparison with previous setups for similar samples. © *2006 American Institute of Physics.* [DOI: 10.1063/1.2194518]

I. INTRODUCTION

Wave propagation at a surface occurs in a wide range of different physical situations, and ease of inspection from above the surface allows one to investigate the two-dimensional propagation of waves and their interaction with discontinuities. Waves on liquids, surface-localized electromagnetic waves, or surface acoustic waves are examples that immediately spring to mind. Optical sensing of such wave fields is facilitated by the simple geometry for optical detection in a transparent medium, such as air, in contact with the propagation medium. Surface motion or strain-induced refractive index changes, in particular, provide suitable mechanisms for the optical sensing of surface acoustic waves (SAWs) on solids with visible optical wavelengths.[1–17] Developments in this field have been driven by the possibilities for nondestructively monitoring SAW propagation for the characterization of the elastic properties of isotropic and anisotropic materials, the mechanical properties of thin films, and SAW devices such as filters.[15–20] Moreover, the imaging of SAW propagation on crystals is of fundamental interest because of the complex focusing patterns that arise from the variation of sound velocity with propagation direction.[1–6]

Various optical detection techniques for SAW have been proposed: knife-edge techniques,[13–15] interferometric techniques,[4–6,17,18,21,22] holographic techniques,[7,8,10–12,15] Schlieren techniques,[16] diffraction techniques,[19] and Brillouin scattering techniques.[15,23] Full information on the SAW field for a general broadband wave disturbance can be most simply obtained by real time detection, and the knife-edge and interferometric techniques have proved most successful for this. Interferometric detection allows the measurement of absolute optical phase, facilitating the calibration of surface displacements. SAW frequencies up to ~1 GHz and wavelengths down to ~1 μm can be investigated using visible light focused to diffraction limited spots.

In this article we present an ultrashort-pulsed optical technique involving a Sagnac interferometer. We apply it to the detection of SAW on opaque substrates, but the method is general and can be used to monitor other surface waves that interact with light. This detection method is viable when synchronized with the source of excitation of the waves to be imaged, and here we use ultrashort light pulses for the SAW excitation as well as for the detection. Incorporation of a two-axis tilt mirror in the system allows two-dimensional scanning. This technique represents a significant advance compared to related methods we have developed[4,5] in that it provides maximum spatial resolution with the use of a single microscope objective lens for both generation and detection of the SAW in opaque substrates. Moreover, we present an optimized Sagnac interferometer that is compensated for optical beam divergence. The system is demonstrated for representative isotropic and anisotropic substrates.

In Sec. II we describe the Sagnac interferometer, the optical scanning system, and the means for evaluating the optical focusing. In Sec. III we describe our experimental results and we conclude in Sec. IV. Appendix A describes the theory of the interferometer and Appendix B the derivation of the shot noise.

[a)]Author to whom correspondence should be addressed; electronic mail: assp@kino-ap.eng.hokudai.ac.jp

II. IMAGING TECHNIQUE

A. Optical interferometer

The present interferometer design is related to a time-domain Sagnac interferometer first developed for monitoring picosecond longitudinal acoustic pulses in solids[24] and then applied to SAW imaging.[5] Sagnac interferometers, inherently of common-path design with no moving parts, have the advantage of mechanical stability. In contrast, for example, Michelson or Mach-Zehnder interferometers are more sensitive to mechanical noise and require an active stabilization or a modulation technique.[22,25–27] Sagnac interferometers based on fiber optics have previously been successfully used to monitor bulk ultrasonic waves in the megahertz frequency range.[28–31] The inherently passive Sagnac interferometers presented here can be used for measuring or imaging small changes in optical reflectivity or phase over a wide frequency range up to 1 THz or above. We present two related Sagnac interferometer designs and explain their respective advantages.

The Sagnac interferometers we use operate in reflection mode at normal incidence with pulsed (probe) light and are convenient for the investigation of opaque samples subject to small changes in optical reflectivity or phase induced by excitation (pump) pulses. (This type of measurement is termed the optical pump and probe technique.) In this article we focus on the application to SAW detection, but changes caused by variations in temperature, carrier concentration, or surface melting, for example, can also be monitored if desired.[32–34]

Figure 1(a) shows the top view of one design, termed configuration A, that we shall discuss first. The probe beam, composed of a train of optical pulses incident from the left in the figure, is linearly polarized at 45° to the x axis (defined as shown in the plane of the paper). The beam is split into vertical and horizontal polarizations, termed probe beams 1 and 2, respectively, by a first polarizing beam splitter (PBS1). The paths of these two probe beams and their polarizations are shown separately in Fig. 2. As shown in Fig. 2(a) the probe beam 1 first travels to a mirror M1 through a quarter-wave plate (QWP1—oriented at 45°) that converts it to circular polarization; after reflection from M1 and second passage through QWP1 its polarization switches to horizontal. Probe beam 1 then traverses PBS1, passes through QWP3 (for conversion to circular polarization), and is focused onto the sample through a microscope objective lens. This beam then traces the route shown in Fig. 2(b). It returns to the nonpolarizing beam splitter (NPBS) with horizontal polarization, is reflected off it, and traverses QWP4 (oriented at 0°). A second polarizing beam splitter PBS2 oriented at 45° then splits the beam equally into two detectors (PD1 and PD2).

The probe beam 2 follows the routes shown in Figs. 2(c) and 2(d), first being reflected off M2 before incidence on the sample. The length of the arm PBS1-M2 is arranged to be longer than the arm PBS1-M1 by a chosen amount to ensure that probe beam 2 arrives at the sample after probe beam 1. (The aim here is to make a differential measurement by comparing the reflectance of the sample at the times of arrival of the optical probe pulses 1 and 2.) Probe beam 2 is guided to the photodetectors where optical interference with probe beam 1 can occur because of the common-path arrangement. The role of QWP4 is to introduce a phase difference of $\pi/2$ between the two probe beams in order to set the interferometer at the position of maximum phase sensitivity, whereas the role of the final polarizing beam splitter PBS2 is to recombine the probe beams (of orthogonal polarization before

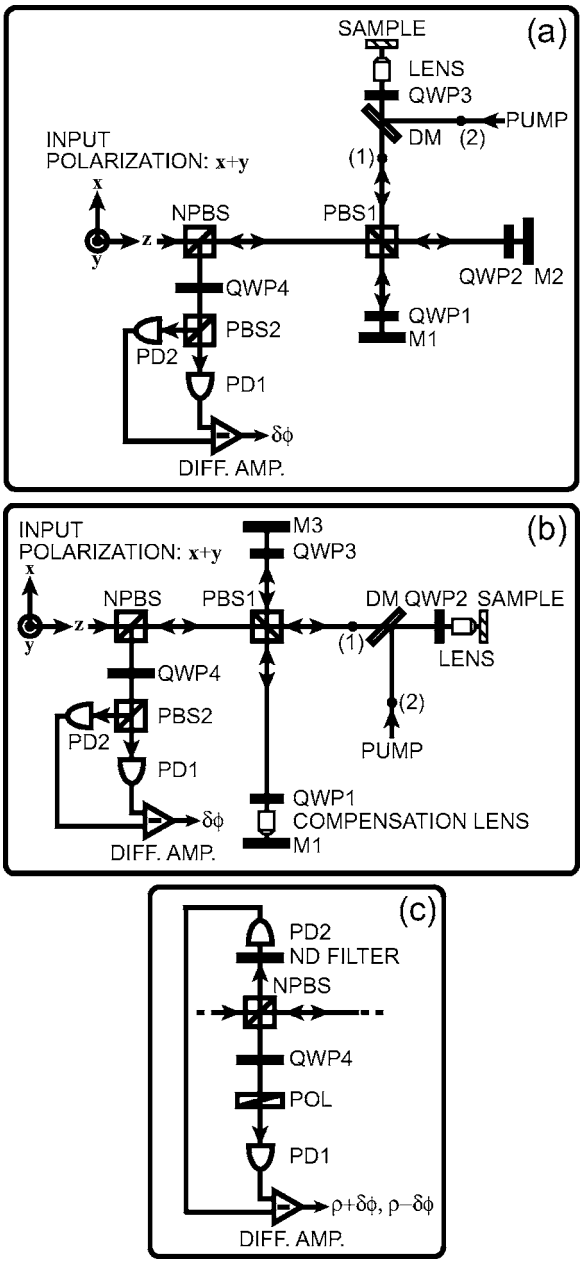

FIG. 1. (a) Schematic top view of configuration A of the Sagnac interferometer designed for optical phase difference ($\delta\phi$) detection. The following abbreviations are used: DM: dichroic mirror, QWP: quarter-wave plate, PBS: polarizing beam splitter, NPBS: nonpolarizing beam splitter: PD: photodetector, DIFF. AMP.: differential amplifier, and POL: polarizer. (b) The configuration B of the interferometer, also designed for phase difference detection, makes use of two microscope objective lenses in order to compensate for beam divergence. The optical scanning system is set at position (1) when it is desired to scan the probe beam. It is also possible to set the optical scanning system at position (2) when it is desired to scan the pump beam. (c) Detector arrangement used when the quantities $\rho+\delta\phi$ or $\rho-\delta\phi$ are monitored separately. ND filter refers to a variable neutral density filter.

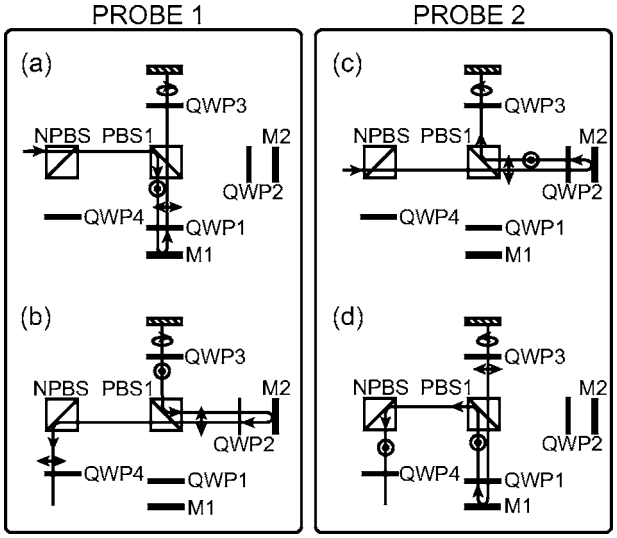

FIG. 2. A schematic diagram of the light path in the configuration A of the Sagnac interferometer. (a) and (b) show in temporal order the passage of the initially vertically polarized probe beam 1 through the system. (c) and (d) show the same for the initially horizontally polarized probe beam 2. The final PBS and photodetectors are omitted here.

PBS2). Because of the common-path arrangement, the exact temporal coincidence and interference of the two probe pulses after PBS2 are guaranteed whatever the coherence length of the light. (Further details of the coherence length are given below.)

Variations in the optical phase difference between probe beams 1 and 2 are monitored by taking the difference in output voltages of the two photodetectors using a differential amplifier. Alternatively, the simpler photodetector setup of Fig. 1(c) may be used with a polarizer (POL) oriented at 45° or 135°, as explained in detail below, although in this case the output is related to both the real and the imaginary parts of the reflectance change. In both detection schemes, the subtraction of the output voltages allows the effects of laser intensity noise fluctuations to be greatly reduced.[35] As an alternative to the orientations of QWP4 and PBS2 described above, it is also possible to arrange for QWP4 to have its optical axis orientated at 45° and for PBS2 or POL to be orientated at 0°. When using PBS2 this is more convenient to arrange on the optical bench.

The SAWs are generated in the opaque sample by a train of pump optical pulses synchronized with the probe pulses, but of different wavelengths. The simplest setup for this purpose, implemented here, involves the use of a second harmonic generation (SHG) crystal to double the frequency of the laser beam. These optical pulses are introduced with a dichroic mirror (DM) and are focused through the same objective lens as the probe pulses. The pump beam is chopped and the output of the differential amplifier is detected synchonously in a lock-in amplifier. This allows the direct detection of changes in the reflectance induced by the pump beam. The resolution of this setup, the detailed optics of the lateral scanning system for the optical beams, and the method to control the beam divergence are described later in this section, in Sec. II B, and in Sec. II C, respectively.

A Jones matrix approach can account quantitatively for the operation of the interferometer (see Appendix A). With the axes defined as shown in Fig. 1, the incident probe beam is polarized in the $\mathbf{x}+\mathbf{y}$ direction, where $\mathbf{x}$ and $\mathbf{y}$ are orthogonal unit vectors. After reflection from the NPBS, with axes defined as in Fig. 1, the (dimensionless) electric fields can be expressed as the Jones vector $(1/2)(r_2\mathbf{x}+r_1\mathbf{y})$, where r_1 and r_2 are the complex amplitude-reflection coefficients of the sample at times τ and $\tau+\delta\tau$. Here τ and $\tau+\delta\tau$ are the times of arrival (with respect to the corresponding pump pulse) of the probe pulses in probe beams 1 and 2, respectively. For example, the Jones vector describing the probe light after passage through QWP4 and POL in the simple setup of Fig. 1(c), when the latter is aligned at 45° to the x axis, is given by

$$\mathbf{E} = \frac{(-r_1 + ir_2)}{4}(\mathbf{x}+\mathbf{y}). \tag{1}$$

As expected, the polarizer POL has combined the electric field components from probe beam 1 (proportional to r_1) and probe beam 2 (proportional to r_2). Similarly, the analogous expression after passage through POL aligned at 135° is given by

$$\mathbf{E} = \frac{(-r_1 - ir_2)}{4}(\mathbf{x}-\mathbf{y}), \tag{2}$$

resulting in a sign change in the combination of the two electric field components compared to Eq. (1).

We are concerned with the measurement of small changes in reflectance $|(r_j - r)/r| \ll 1$, where $r = r_0 \exp(i\phi_0)$ is the sample reflectance in the absence of the pump pulses and r_j is the reflectance of the probe beam $j=1,2$. It is convenient to write $r_j = r_0(1+\rho_j)\exp[i(\phi_0+\delta\phi_j)]$, where ρ_j ($\ll 1$) is the relative change in the real part of the reflectance and $\delta\phi_j$ ($\ll 1$) is the change in phase at times τ ($j=1$) and $\tau+\delta\tau$ ($j=2$) induced by the pump pulses. It is straightforward to show that these definitions are consistent with the expression $(r_2-r_1)/r \approx (\rho_2-\rho_1)+i(\delta\phi_2-\delta\phi_1)$ to first order in small quantities. For a given $\delta\tau$, ρ_j and $\delta\phi_j$ are functions of τ.

With these definitions, Eqs. (1) and (2) can be used to evaluate the time-averaged optical intensities that control the voltage output of the photodetector PD1. This results in voltage outputs proportional to $1+\rho+\delta\phi$ and $1+\rho-\delta\phi$ for POL orientations 45° and 135°, respectively, where $\rho=\rho_1+\rho_2$ and $\delta\phi=\delta\phi_2-\delta\phi_1$. In the detector configuration of Fig. 1(a), these two outputs are obtained simultaneously and the output of the differential amplifier is proportional to the quantity $\delta\phi$ (referred to as the optical phase difference here).

The main mechanism for SAW detection is through the optical phase difference, which normally contains a dominant contribution from the difference in outward surface displacement δz at the times of arrival of the two probe pulses, where $\delta\phi = -4\pi\delta z/\lambda$. Here λ is the central wavelength of the optical probe beams. However, the strain field associated with the SAW modulates the dielectric constants of the sample through the photoelastic effect and this also induces changes in reflectance. For the SAW frequencies in question here (below ~1 GHz), these photoelastic changes in reflectance in metals at visible or near-infrared optical wavelengths are usually much smaller than those caused by sur-

face displacement. In contrast, at higher acoustic frequencies (above ~100 GHz) the photoelastic changes in metals are often comparable to those caused by surface displacement (as demonstrated, for example, for the case of bulk longitudinal waves[36,37]). The surface displacement is comparable in both frequency ranges but the strain, and hence the photoelastic contribution (for a given optical probe penetration depth), is proportional to the inverse of the acoustic wavelength. This implies a smaller influence of the photoelastic effect at lower acoustic frequencies in metals. Nevertheless, it is possible to image SAW through the changes in reflectivity (or, equivalently, ρ) by means of this photoelastic coupling.[38,39] Such photoelastic changes could be exploited to image shear components of SAW traveling parallel to surfaces.

The relative timing of the two probe pulses and the pump pulse can be varied at will. For SAW detection in the frequency range of 100 MHz–1 GHz we typically work with acoustic pulse durations ~1 ns. In this case, the time interval between the two probe pulses $\delta\tau$ is chosen small enough ($\lesssim$1.5 ns) for the detected acoustic pulses not to appear broadened.[40] If a value of $\delta\tau$ much smaller than this is chosen, the output of the interferometer effectively becomes a derivative function. For example, for the setups of Fig. 1(a) or 1(b), the output for small $\delta\tau$ is proportional to the time derivative of the optical phase change. However, if $\delta\tau$ is chosen at too small a value then the detected signals are significantly reduced. For SAW detection we therefore generally work with $\delta\tau$ in the range of ~0.3–1.5 ns.

It is, however, in general also possible to work with much longer values of $\delta\tau$, timing the first probe pulse to always arrive before each pump pulse and the second probe pulse after;[24,41–43] in this case one can approximate r_1 as a time-independent quantity. (Alternatively, if desired, the interval $\delta\tau$ can be scanned.) The present interferometer design (configuration A) has the advantage that it is possible to adjust $\delta\tau$ to an arbitrarily small value by simple axial displacement of mirrors M1 or M2. In contrast, in the previous design[24] the minimum value of $\delta\tau$ is determined by the size of the beam splitters. Another advantage is that the present design requires only one NPBS and one PBS in the main body of the interferometer, compared with one NPBS and two PBSs for the previous version, allowing for a more compact construction and easier alignment.

The present and previous designs of the interferometer suffer from losses owing to the use of a NPBS in which approximately half the optical probe beam power is wasted on each pass. Further losses occur from the double transmission through the objective lens and other optical components, and from the reflection from the sample. The loss from the NPBS can, in fact, be avoided by the introduction of Faraday rotators into the interferometer,[44] but for most applications this gain does not justify the extra complication.

We now describe relevant details of the optical system used in conjunction with the interferometer: for the optical source we use a mode-locked Ti:sapphire femtosecond laser system (Coherent, Mira 900) delivering ~100 fs duration infrared optical pulses at a repetition rate f=76 MHz. This optical pulse duration corresponds to an optical coherence length of ~30 μm. We have chosen to operate with optical pump and probe pulses at the wavelengths of 415 and 830 nm, respectively. Both pump and probe pulses are focused to ~2 μm diameter spots on the sample surface using a microscope objective lens, as described in detail in the next section. An acousto-optic modulator is used to chop the optical pump beam at 1 MHz. (This frequency should be sufficiently high, up to a maximum of $f/2$, because the laser intensity noise decreases with increasing frequency.) The choice of the chopping frequency is limited in our case by the response of the acousto-optic modulator and the photodetectors. The probe beam is guided through an eight-pass 0.5 m optical delay line to produce up to ~13 ns of optical delay. The optical beam diameter is increased to ~1 cm for this purpose to avoid problems of variable beam divergence during the scanning process.[45] The passage of the optical pump and probe beams through the optical system lead to increased optical pulse durations that reduce the temporal resolution to ~1 ps. Although it is straightforward to use optical pulse-compression techniques to restore the original ~100 fs time resolution, 1 ps is perfectly acceptable for SAW imaging on nanosecond time scales.

The average optical probe beam power at the photodetector PD1 is ~75 μW, whereas ~1.2 mW is incident on the sample (the difference being due to the losses mentioned above). We obtain a resolution in the measured phase difference $\delta\phi \sim 5\times10^{-6}$. This noise level is not sensitive to the exact value of $\delta\tau$ chosen (here ~1 ns). Comparing this with the expression for shot noise, as described in detail in Appendix B, we find that the noise level (at the chosen bandwidth of ~300 Hz) is approximately at the shot noise limit. The present noise level allows us to obtain, for example, a 300×300 pixel image of the SAW propagation in 5 min. Moreover, the apparatus is sufficiently stable over the period of time required to obtain a full animation of typically 10–40 images covering the 13.2 ns laser repetition period. The bandwidth for detection is chosen to be approximately equal to the reciprocal of the time required to scan one pixel of the image. The above image acquisition conditions therefore correspond to a bandwidth of 300 Hz and the lock-in amplifier time constant is set to the inverse of this (3 ms).

For our probe wavelength a phase change of 5×10^{-6} corresponds to an out-of-plane surface displacement of ~0.5 pm at ~300 Hz bandwidth.[46] This resolution was achieved with a measurement system including the following instruments: photodetectors containing reverse-bias Si p-i-n photodiodes (Hamamatsu: S3072), an acousto-optic modulator (Hoya-Schott: A-160-488), and a lock-in amplifier (Stanford Research Systems: SR844).

The contrast of the interferometer is limited by the nonreciprocal Gaussian beam optics of the paths of the probe beams 1 and 2; because these beams pass through the objective lens after traversing different lengths inside the interferometer, the angular divergence of the beams on optical interference at the photodetectors will be slightly different. With the ~2 mm diameter optical beams used in our setup, limited by the aperture of the microscope objective lens, we can routinely achieve ~90% contrast. This limitation in contrast is also influenced by errors in alignment and residual reflec-

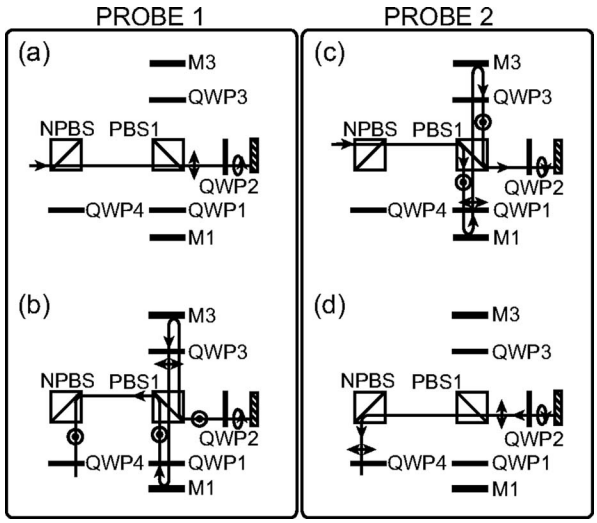

FIG. 3. A schematic diagram of the light path in the configuration B of the Sagnac interferometer. (a) and (b) show in temporal order the passage of the initially horizontally polarized probe beam 1 through the system. (c) and (d) show the same for the initially vertically polarized probe beam 2. The final PBS and photodetectors are omitted.

tions from interfaces. The contrast can be checked by rotating the quarter-wave plate QWP4 about its axis and monitoring the intensity of the two photodetectors. The response of the photodetectors as a function of the polarizer angles is discussed theoretically in Appendix A.

The nonreciprocity of configuration A as regards the Gaussian beam optics can be overcome by a slight modification. This is implemented in configuration B, as shown in Fig. 1(b). The details of the light path are shown in Fig. 3. Configuration B differs from configuration A in the position of the sample and in the presence of a compensation lens in front of M1. Probe beams 1 and 2 are, respectively, initially horizontally and vertically polarized in this configuration. As is evident by examination of the beam paths in Fig. 3, reciprocity is now strictly maintained provided that the two arms containing M1 and the sample are arranged to be identical (apart from the difference between the material of the sample and M1). This arrangement has the advantage of potentially allowing a higher contrast. In practice, however, we found that other factors limited the contrast of the interferometer and that 90% contrast was the best we could obtain. One limiting factor, apart from alignment and residual reflection errors, is a spectral dependence of the retardation of QWP4 that influences the contrast due to the finite optical bandwidth ($\sim$20 nm in wavelength) of the optical probe pulses.

Configuration B is less suited to an arbitrary choice of the time delay $\delta\tau$ between the two probe pulses. The minimum value of $\delta\tau$ is determined by a double pass through the arms containing M1 and M2 of the interferometer. For this reason configuration B is less convenient for imaging SAW in the 100 MHz–1 GHz frequency range with a relatively short duration $\delta\tau$ (e.g., $<$0.5 ns) between the two probe pulses. It is, however, possible to deliberately choose a value of $\delta\tau$ that is large compared to the required temporal measurement interval, and thereby measure the SAWs through variations in only one of the probe beams. This alternative method, that essentially monitors the surface displacement,

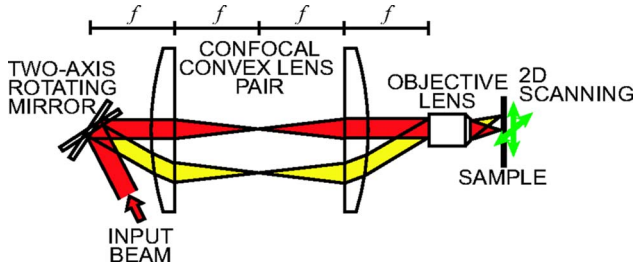

FIG. 4. (Color online) Schematic diagram of the 4f lens system. Examples of optical beam paths for two different angular positions of the rotating mirror are illustrated. The axis of rotation of the mirror is on the optical axis.

would be convenient for imaging SAW in the 100 MHz–1 GHz frequency range with a pulsed laser whose repetition rate is significantly lower than the one (76 MHz) used in this study. The SAW images presented in this article are obtained with configuration A.

B. Optical scanning system

The principal requirements of the two-dimensional optical scanning system are (i) operation for opaque substrates with access from a single side of the sample and (ii) maximum lateral spatial resolution. A two-lens system for optical generation and detection based on a Sagnac interferometer was previously used to image SAW on opaque substrates,[4] but the lateral resolution is limited because of the requirement for oblique incidence for one of the optical beams. Here we incorporate a two-axis rotating mirror to allow optical generation and detection of SAW by the use of a single objective lens. We combine this with a 4f lens system (see, for example, Refs. 21 and 47) incorporating a confocal convex lens pair with focal lengths f=100 mm, as shown in Fig. 4. The 4f design has two important advantages: it allows one to change the angle of incidence on the objective lens without (i) laterally translating the beam and (ii) without changing the beam collimation. The complete optical system consists of an automatically controlled two-axis rotating mirror (Sigma Koki, MINI-5D and DMY-10) followed by the convex lens pair and a microscope objective lens (Olympus SLMPlan 50$\times$ with a working distance of 15 mm). By raster scanning the mirror angles, a two-dimensional image can be formed through point-by-point measurement. This optical scanning system can be incorporated in the interferometer at position (1) in Fig. 1 for purposes of scanning the probe beam. It is, however, also possible to scan the pump beam, in which case the scanning system is placed at position (2). Experimental results for both cases will be presented in Sec. III. In the case of scanning the probe beam, the reciprocity of the interferometer configuration can be improved, if required, by adding an additional confocal lens pair (identical to that of the optical scanning system) at the equivalent point in the other path of the interferometer.

The variation in the angle of incidence at the objective lens is determined by the angles of mirror rotation (see Fig. 4). The optical spot position in the focal plane of the objective lens is determined by its focal length Λ and the angles of incidence ξ and ζ defined in Figs. 5(a) and 5(b). The vector $\mathbf{\Gamma}=(x,y)$ describing the lateral position of the focal point is

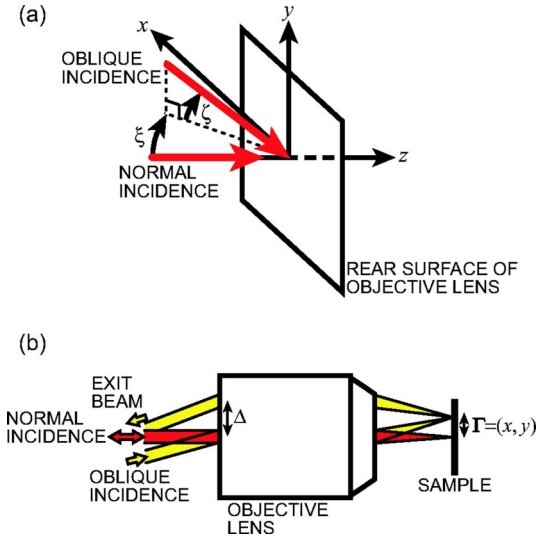

FIG. 5. (Color online) (a) The definition of the two angles of incidence ξ and ζ at the rear surface of the objective lens. (b) Schematic diagram to show how the optical beams are reflected from the sample. The lateral shift Δ in the position of the exit beam limits the maximum scan area.

given by $(-\Lambda\xi,-\Lambda\zeta)$. For our choice of $\Lambda=3.6$ mm, an angular variation of $\sim 0.01\pi$ $(\sim 1.6°)$ is required for a 100 μm spot displacement in the focal plane. The imaging area is limited by the shift in the beam path on reflection from the sample due to the clipping of the exiting beam (of diameter ≈ 2 mm) by the aperture (diameter $D=3$ mm) of the objective lens, as shown schematically in Fig. 5(b). In order to keep the lateral beam shift $\Delta=2\Gamma$ in the range $\Delta<D/3$, for example, the maximum (square) imaging area is limited to $D/6\times D/6$, corresponding to an area of 500×500 μm^2 in our case. We found that this order of lateral beam shift had no detectable effect on the interferometer contrast when scanning the probe beams; bearing in mind that both probe beams 1 and 2 are affected identically by this shift, this is not surprising. In addition, the combined effects of spherical and chromatic aberration[48] for the scanned beams do not result in any significant change in beam quality during scanning for the temporal resolution $(\sim 1$ ps) and spatial resolution $(\sim 2$ μm) concerned. In this connection we noted that there was no detectable change in spot size of the scanned beam during the scanning.

The required beam deflection angles ξ and ζ are related to corresponding angles describing the rotating mirror orientation. The two independent axes of rotation of the mirror are chosen to correspond to the azimuthal and elevation angles of deviation, θ and ϕ, defined in Fig. 6. We denote the angle of incidence of the light on the rotating mirror in its central position as α, for which the two angles of deviation, ξ and ζ, are equal to zero. The angles ξ and θ are related through $\xi=2\theta$.[49] In addition, since θ and ϕ are small, $\zeta=2\phi\cos\alpha$. (This can be seen by inspection of the case for which $\theta=0$, for example.) The small values of θ and ϕ $(\sim 1°)$ also imply that any effects of spherical aberration are negligible. In order to calibrate the horizontal and vertical displacements x and y on the sample, we make use of the following equation relating these displacements to the tilt angles: $\mathbf{\Gamma}=(x,y)=(-2\Lambda\theta,-2\Lambda\phi\cos\alpha)$, where Λ and α are known.

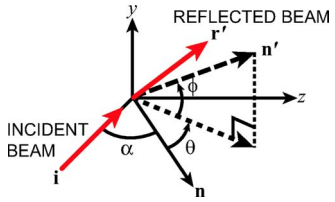

FIG. 6. (Color online) Definition of the angles of α, θ, and ϕ representing, respectively, the angle of incidence on the mirror in its initial position, the azimuth angle of the rotating mirror, and the elevation angle of the rotating mirror. The vector $\mathbf{r}'$ refers to a unit vector in the direction of the reflected light beam, whereas $\mathbf{n}$ and $\mathbf{n}'$ refer to the unit normals to the mirror. The unprimed and primed symbols refer to the mirror in its central and tilted positions, respectively. The unit vector $\mathbf{i}$ refers to the direction of the incident light. The angles θ and ϕ are exaggerated in size for clarity.

For ease of spot alignment, a 1 mm glass plate is positioned between the objective lens and the nearest quarter-wave plate at an angle of 45° to sample the beams reflected from the sample. This system, combined with a white light source and a charge-coupled device (CCD) camera, allows an image of the scanned area to be viewed during the measurement process.

C. Beam divergence control

A problem arises in the use of a single objective lens for focusing two light beams of different wavelengths because of chromatic aberration. The difference in focal lengths at the pump and probe wavelengths (415 and 830 nm, respectively) is approximately 10 μm in our setup. This difference should be compensated if micron-order spatial resolution is desired. For this purpose we insert a coaxial convex lens pair (each lens of focal length 100 mm) in the pump beam path before the dichroic mirror in order to control the beam divergence and to bring the pump beam focus to the same plane as the probe beam focus. In order to improve beam quality we also insert spatial filters consisting of confocal lens pairs and pinholes into the pump and probe beams after passage through the SHG crystal.

In order to characterize the focusing characteristics of the setup, we measured the beam intensity profiles in the beam propagation (z) direction in the region of the focus, in particular, the full width at half maximum (FWHM). This is done by scanning a knife edge horizontally and vertically through the beams while monitoring the throughput with a photodetector, and assuming that the beam shape can be described by an elliptical Gaussian.[50] Typical results are shown in Fig. 7 for the case in which the alignment is optimal. One can see that the minimum diameters for both beams are obtained at essentially the same z position, in which case both beams are circular. The diameter of both pump and probe beams is ~ 2 μm (FWHM of intensity) at this position. This value is three times smaller than that of our previous setup for opaque samples.[4] These optical pump and probe spot sizes are used in the experiments of Secs. II C and III.

A further improvement in lateral spatial resolution could be obtained by the use of an objective lens with higher magnification at the expense of a smaller scanning area. However, even if all aberration effects are successfully compen-

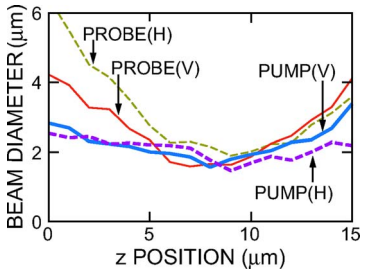

FIG. 7. (Color online) Measured FWHM beam diameters as a function of position in the beam propagation direction. The thin and thick lines refer, respectively, to the probe and pump beams. The dotted and solid lines refer, respectively, to horizontal and vertical beam profiles.

sated for in this case, the longer-wavelength beam (in this case the probe) will become the limiting factor because of the diffraction limit.

III. SURFACE ACOUSTIC WAVE IMAGING

We present here two typical examples of SAW imaging using the configuration A of the interferometer. We first describe the results for the configuration in which pump beam is scanned. The images obtained with this configuration are based on a changing optical excitation point on the sample and are somewhat less easy to interpret for (elastically, thermally, or optically) laterally inhomogeneous samples. For laterally homogeneous samples, such as single crystals, it is irrelevant which optical beam is scanned. In this article we shall demonstrate the interferometer operation in both configurations with laterally homogeneous samples for simplicity.

We first present data for the (100) surface of a single-crystal silicon wafer of thickness 1 mm coated with a polycrystalline gold film of thickness 50 nm. This sample was previously used for measurements at lower spatial resolution using a two-objective-lens system.[4] The optical pump pulse energy incident on the sample is 0.1 nJ (or an average chopped pump beam power of 5 mW). The temporal separation of the two optical probe pulses for this measurement is 1.33 ns. The simple detection system of Fig. 1(c) was used and the data correspond to an image of the quantity $\rho - \delta\phi$. A snapshot of the propagating SAW at 1 ns after generation for a 310×300 μm^2 region is shown in Fig. 8(a). This image of 150×938 pixels was obtained in $\sim$10 min ($\sim$4.5 ms/pixel with a lock-in amplifier time constant of 3 ms). The angle of incidence on the scanning mirror α was set equal to 15° for this experiment and the scanning direction in this image is vertical for the long stroke of the raster scans. The pump spot corresponds to the point at the center of the ripple pattern. Wave fronts characteristic of the fourfold symmetry of the elastic properties of the silicon substrate are clearly visible (see, e.g., Ref. 51). (The [011] direction is parallel to the y axis.) The smaller ripples are associated with the frequency-dependent elastic dispersion of the thin film system.[4]

Figures 8(b) and 8(c) show line scans corresponding to horizontal and vertical sections of Fig. 8(a) (for lines crossing the pump spot position). These data show that SAWs appear as broadband pulses, with a typical frequency of 500 MHz, wavelength $\sim$10 μm, and phase velocity

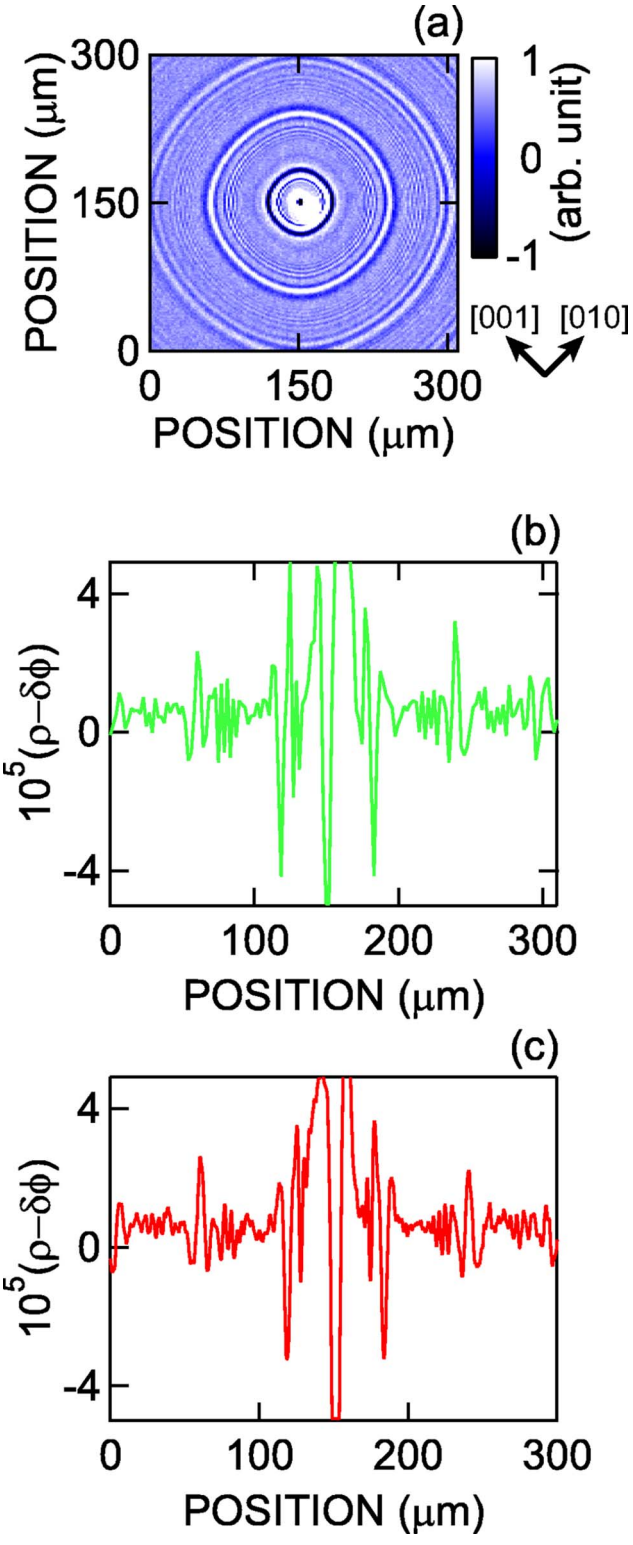

FIG. 8. (Color online) (a) A snapshot of the SAW propagation over a 310×300 μm^2 region of a silicon (100) surface covered with a 50 nm polycrystalline gold film. The data are obtained by scanning the pump beam spot. Horizontal and vertical cross sections of (a) are shown in (b) and (c), respectively, for lines crossing the pump spot position.

$\sim$5.2 km s^{-1}. The detailed acoustic spectrum for such thermoelastic generation is described elsewhere.[5,6] As explained in Sec. II A, the SAWs are detected through the outward surface motion of the sample, which only contributes to the quantity $\delta\phi$. The typical surface displacement caused by the

propagating SAWs is ~5 pm. (A detailed thermoelastic analysis of the generation process, which should include the effect of the thin film, is beyond the scope of this article.) However, the peak at the position of the pump spot contains a significant contribution from the quantity ρ because of temperature-induced changes in the sample dielectric constants at this point. The ~2 μm lateral spatial resolution of the image is determined by the probe spot size.[52]

By changing the value of the delay time, one can build up animations of the SAW propagation. An animation corresponding to the above data can be viewed elsewhere.[53]

We next describe the results for the configuration in which the optical scanning system is placed in the probe beam. In this configuration the optical excitation point is fixed and so a single wave field is being imaged. We present data for a sample of crown glass of thickness 1 mm coated with a polycrystalline gold film of thickness 60 nm. The excitation and probing conditions are the same as above (except that α was set to 42° here). The results are shown in Fig. 9 for a 200×130 μm^2 region at a time approximately corresponding to that of the pump pulse arrival at $t=0$ (that is, arriving at a time between the two probe pulses). This image of 200×833 pixels was obtained in 10 min (corresponding to ~3.5 ms/pixel with a lock-in amplifier time constant of 3 ms). In this case the sample is isotropic (at least in the lateral direction) and so the wave fronts show circular symmetry. The SAWs again appear as broadband pulses, with a typical frequency of 300 MHz, wavelength ~10 μm, and phase velocity ~3.1 km s^{-1}. Figures 9(b) and 9(c) show the central horizontal and vertical line scans. Again SAW frequency-dependent dispersion effects are clearly visible and the frequency spectrum is similar to that of silicon above. The lateral resolution is the same as for the case of scanning the pump beam.

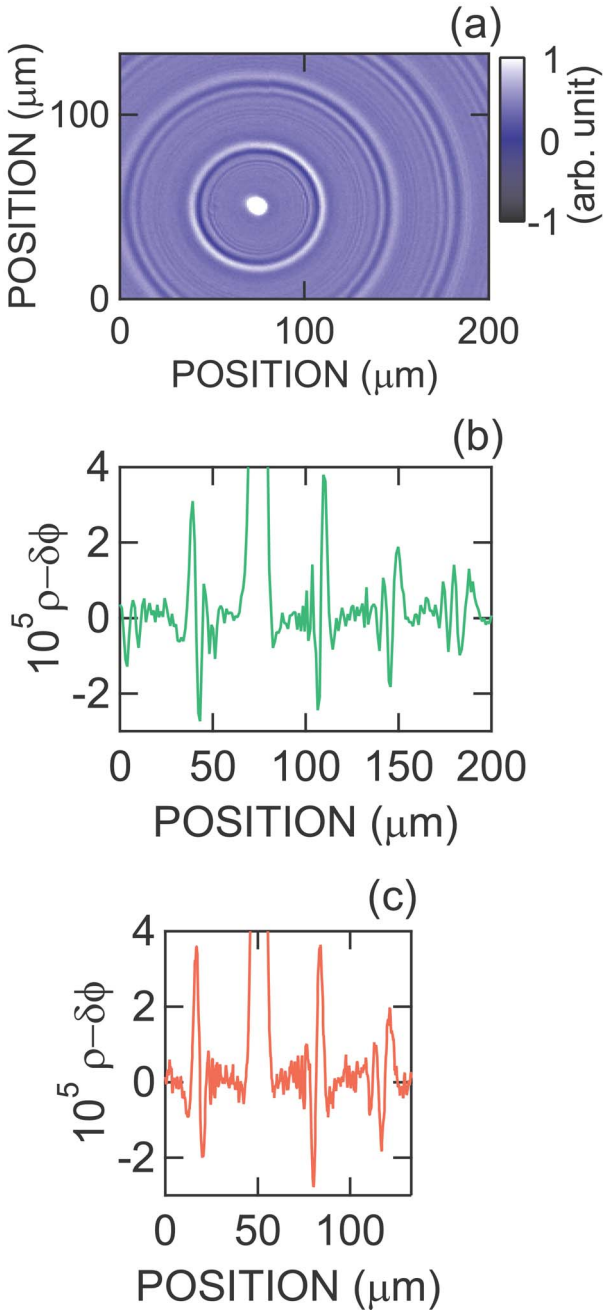

FIG. 9. (Color online) (a) A snapshot of the SAW propagation over a 200×130 μm^2 region of a crown glass substrate covered with a 60 nm polycrystalline gold film. The data are obtained by scanning the probe beam spot. Horizontal and vertical cross sections of (a) are shown in (b) and (c), respectively, for lines crossing the pump spot position.

IV. DISCUSSION

In conclusion, we have described in detail the construction and operation of scanning ultrafast Sagnac interferometers for imaging surface wave propagation. We show how this is achieved with the use of an optical scanning system incorporating a single microscope objective lens for pulsed optical excitation and detection. Results for SAW imaging on opaque media are demonstrated with ~2 μm lateral spatial resolution. This system shows great promise for the imaging of a variety of SAW systems such as resonators, waveguides, or phononic crystal structures. Moreover, it is also applicable to the study of bulk waves impinging on surfaces whenever the near-surface strain induces an outward displacement.

The system is not restricted to SAW imaging but can be applied to a variety of other surface wave propagation phenomena or diffusion phenomena. One possibility is the application to the imaging of surface plasmons in thin metal films on dielectrics through the coupling of the metal dielectric constants to temperature changes (caused by the surface plasmon dissipation). Another example that exploits temperature coupling is the monitoring of lateral thermal diffusion on ultrashort time scales; one could study transient heat flow distributions on the surface of microstructures or heat sinks. Similarly, the lateral diffusion of carriers in semiconductor heterostructures could be imaged through the coupling of the dielectric constants to carrier density.

The method relies on a source of optical probe pulses that are synchronous with the excitation. The excitation in the present article is also optical, but non-optical excitation is equally viable provided it is synchronous. One example would be in the monitoring of piezoelectrically driven SAW devices based on interdigital transducers. Our technique is most conveniently used with pulsed excitation. However, since spatiotemporally resolved data are obtained, by taking the temporal Fourier transform of these data the response at

any single frequency in the excitation spectrum can be obtained. Moreover, by in addition taking the two-dimensional spatial Fourier transform, the dispersion relation of the surface wave propagation can be derived.[6] It is also possible to control the repetition rate of the optical pulses using a pulse picker to allow a variable recovery time for the sample to excitation. The frequency of operation of the interferometer is limited at high frequencies to the inverse of the optical pulse duration, and operation up to 50 THz should be relatively straightforward. However, the frequency of laterally propagating SAWs that can be detected is limited by the optical spot sizes, so that in practice it is difficult with diffraction limited optics to make such SAW measurements much above 1 GHz. At low frequencies one is limited in signal acquisition time by the length of the optical delay line. A 10 m optical delay line would allow frequencies as low as ~30 MHz to be probed, for example.

Although in the present article SAWs are mapped essentially through the outward surface displacement, it should also be feasible to image the shear components of SAWs traveling parallel to the surface by means of the generally smaller signals arising from the photoelastic effect. For this purpose it may be sufficient to monitor reflectivity changes only. We are at present investigating this possibility in both isotropic and anisotropic solids. Another interesting extension of our technique would be to the detection of interface waves, such as those between a fluid and a solid, between two solids, or in multilayers.[54–56]

Further improvements in spatial resolution are possible by working with shorter optical wavelengths or higher-power microscope objective lenses. The only requirement for the sample is that it should be smooth enough for specular reflection of the probe light beam. It may also be possible to combine our Sagnac configuration with near-field optical techniques to go beyond the diffraction limit (see, e.g., Ref. 57). The inherent stability of the Sagnac interferometer coupled with the ease of scanning, and the combination with low-cost and compact ultrafast laser systems, makes scanning ultrafast Sagnac interferometry an attractive measurement method for mapping a variety of transient phenomena from nanosecond down to femtosecond time scales.

ACKNOWLEDGMENTS

This work has been partially supported by the 21st century Center of Excellence (COE) program on "Topological Science and Technology" from the Ministry of Education, Culture, Sport, Science and Technology of Japan. One of the authors (T.T.) is a JSPS research fellow. The authors are grateful to Peter van Capel, Madeleine Msall, and Eiji Muramoto for a critical reading of the manuscript.

APPENDIX A: JONES MATRIX AND JONES VECTOR ANALYSIS

A detailed discussion of the Sagnac interferometer based on the Jones matrix formalism[58] is given in this appendix. The convention used for the coordinate system is illustrated in Fig. 10 for the example of normal reflection from a plane surface. The light propagation direction is always defined as the z direction and the coordinate perpendicular to the plane of the interferometer is defined as the y direction. (An exception applies to the beam exiting PBS2 for which x and y are not in the plane of the interferometer.) The orientation angles of the polarizers and wave plates are measured in the clockwise direction from the x direction when facing the direction of light propagation, as shown. Fields are assumed to vary in time as $\exp(-i\omega t)$. The Jones unit vector for x-polarized (horizontally polarized) light is given by

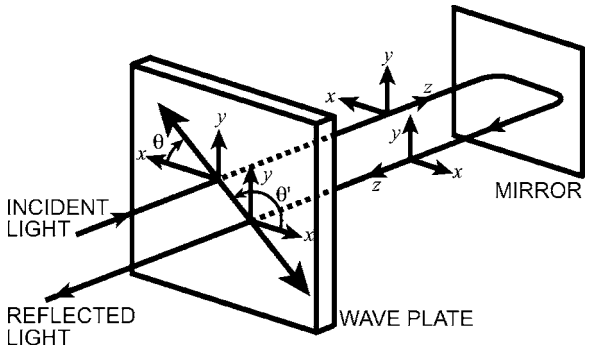

FIG. 10. Schematic diagram showing the definition of the coordinate directions, and also the definition of the optical-component orientation angles, for the example of a wave plate. In this example light is reflected at normal incidence from a flat mirror. The orientation of the fast axis of the wave plate is indicated by the double-headed arrow. θ and θ' refer to the orientation angles for the incident and reflected light, respectively.

$$\mathsf{H} = \begin{pmatrix} 1 \\ 0 \end{pmatrix}, \tag{A1}$$

whereas that for y-polarized (vertically polarized) light is given by

$$\mathsf{V} = \begin{pmatrix} 0 \\ 1 \end{pmatrix}. \tag{A2}$$

With the axes defined as in Fig. 10, the Jones matrix R of a reflector at normal incidence with complex amplitude-reflection coefficient (or reflectance) r is given by

$$\mathsf{R} = \begin{pmatrix} -r & 0 \\ 0 & r \end{pmatrix}. \tag{A3}$$

For the special case when $r=1$ we define $\mathsf{R}=\mathsf{M}$. The Jones matrices for reflection from and transmission through a polarizing beam splitter (PBS) are given, respectively, by

$$\mathsf{PBS}_r = \begin{pmatrix} 0 & 0 \\ 0 & 1 \end{pmatrix}, \tag{A4}$$

$$\mathsf{PBS}_t = \begin{pmatrix} 1 & 0 \\ 0 & 0 \end{pmatrix}. \tag{A5}$$

These also apply to a linear polarizer that is oriented vertically or horizontally, respectively. The Jones matrices for reflection from and transmission through a nonpolarizing beam splitter (NPBS) are given, respectively, by

$$\mathsf{NPBS}_r = \frac{1}{\sqrt{2}} \begin{pmatrix} -1 & 0 \\ 0 & 1 \end{pmatrix}, \tag{A6}$$

$$\mathrm{NPBS}_t = \frac{1}{\sqrt{2}}\begin{pmatrix} 1 & 0 \\ 0 & 1 \end{pmatrix}. \tag{A7}$$

The Jones matrix for a wave plate with its fast optical axis parallel to the x direction is given by

$$\mathrm{WP}_{\Delta,0} = \begin{pmatrix} 1 & 0 \\ 0 & \exp(-i\Delta) \end{pmatrix}, \tag{A8}$$

where Δ is the retardation of the wave plate. If the wave plate is tilted by an angle θ with respect to the x axis (see Fig. 10), the corresponding Jones matrix is given by

$$\mathrm{WP}_{\Delta,\theta} = \begin{pmatrix} \cos\theta & -\sin\theta \\ \sin\theta & \cos\theta \end{pmatrix}\begin{pmatrix} 1 & 0 \\ 0 & \exp(-i\Delta) \end{pmatrix} \times \begin{pmatrix} \cos\theta & \sin\theta \\ -\sin\theta & \cos\theta \end{pmatrix}. \tag{A9}$$

Taking these relations into account, the Jones matrices for a quarter-wave plate (QWP) ($\Delta=\pi/2$) with their fast axis tilted by $\theta=0°$, 45°, and 135° are given by

$$\mathrm{QWP}_{0^\circ} = \begin{pmatrix} 1 & 0 \\ 0 & -i \end{pmatrix}, \tag{A10}$$

$$\mathrm{QWP}_{45^\circ} = \frac{1}{2}\begin{pmatrix} 1-i & 1+i \\ 1+i & 1-i \end{pmatrix}, \tag{A11}$$

$$\mathrm{QWP}_{135^\circ} = \frac{1}{2}\begin{pmatrix} 1-i & -1-i \\ -1-i & 1-i \end{pmatrix}. \tag{A12}$$

Similarly, for the transmission through a polarizer oriented at 45° and 135°, as for the example of POL in Fig. 1(c), one has, respectively,

$$\mathrm{POL}_{45^\circ} = \frac{1}{2}\begin{pmatrix} 1 & 1 \\ 1 & 1 \end{pmatrix}, \tag{A13}$$

$$\mathrm{POL}_{135^\circ} = \frac{1}{2}\begin{pmatrix} 1 & -1 \\ -1 & 1 \end{pmatrix}. \tag{A14}$$

As a concrete example we present here the Jones matrix analysis for the configuration A of the Sagnac interferometer of Figs. 1 and 2. The light incident on the interferometer is linearly polarized with $\theta=45°$ (that is, in the $\mathbf{x}+\mathbf{y}$ direction). The polarizing beam splitter PBS1 splits the incident light into the probe beams 1 (reflected light and vertical polarization) and 2 (transmitted light and horizontal polarization). Using the Jones matrices above, the Jones vector for probe beam 1 after QWP4 is given by

$$\begin{aligned}\mathrm{PROBE1} = {} & \cdot \mathrm{QWP}_{0^\circ} \cdot \mathrm{NPBS}_r \cdot \mathrm{PBS}_t \cdot \mathrm{QWP}_{135^\circ} \cdot \mathsf{M} \\ & \cdot \mathrm{QWP}_{45^\circ} \cdot \mathrm{PBS}_r \cdot \mathrm{QWP}_{135^\circ} \cdot \mathsf{R}_1 \cdot \mathrm{QWP}_{45^\circ} \\ & \cdot \mathrm{PBS}_t \cdot \mathrm{QWP}_{135^\circ} \cdot \mathsf{M} \cdot \mathrm{QWP}_{45^\circ} \cdot \mathrm{PBS}_r \\ & \cdot \mathrm{NPBS}_t \cdot \mathsf{V} = \begin{pmatrix} -r_1/2 \\ 0 \end{pmatrix},\end{aligned} \tag{A15}$$

where R_1 is the Jones matrix for reflection from the sample at a (delay) time for which the sample reflectance is r_1. Similarly, for probe beam 2, the Jones vector for probe beam 2 after QWP4 is given by

$$\begin{aligned}\mathrm{PROBE2} = {} & \cdot \mathrm{QWP}_{0^\circ} \cdot \mathrm{NPBS}_r \cdot \mathrm{PBS}_r \cdot \mathrm{QWP}_{135^\circ} \cdot \mathsf{M} \\ & \cdot \mathrm{QWP}_{45^\circ} \cdot \mathrm{PBS}_t \cdot \mathrm{QWP}_{135^\circ} \cdot \mathsf{R}_2 \cdot \mathrm{QWP}_{45^\circ} \\ & \cdot \mathrm{PBS}_r \cdot \mathrm{QWP}_{135^\circ} \cdot \mathsf{M} \cdot \mathrm{QWP}_{45^\circ} \cdot \mathrm{PBS}_t \\ & \cdot \mathrm{NPBS}_t \cdot \mathsf{H} = \begin{pmatrix} 0 \\ ir_2/2 \end{pmatrix},\end{aligned} \tag{A16}$$

where R_2 is the Jones matrix for reflection from the sample at a time for which the sample reflectance is r_2. Here we have assumed for simplicity that both probe beams 1 and 2 start out as unit Jones vectors (V and H, respectively.)

Interference of the two probe beams can be induced by means of a polarizing beam splitter, as in Fig. 1(a), or a polarizer, as in Fig. 1(c). We discuss the case of the use of a polarizer in detail. When the polarizer is oriented at 45°, the Jones vector after passage through it (just before PD1) is given by

$$\frac{1}{4}\begin{pmatrix} -r_1 + ir_2 \\ -r_1 + ir_2 \end{pmatrix}. \tag{A17}$$

Since the optical intensity is proportional to the square of the absolute value of Eq. (A17), the output from the photodetector PD1 is in this case proportional to the quantity $I_{45^\circ} = (1/8)|-r_1+ir_2|^2$.

For small changes in r_j for $j=1,2$, as explained in Sec. II A, we may write $r_j = r(1+\rho_j + i\delta\phi_j)$, where the small quantities ρ_j and $\delta\phi_j$ are functions of the time delay τ. Therefore, setting $\rho=\rho_1+\rho_2$ and $\delta\phi=\delta\phi_2-\delta\phi_1$, one obtains

$$I_{45^\circ} = (R/4)(1+\rho+\delta\phi), \tag{A18}$$

where $R=|r|^2$ and second-order terms in ρ_j and $\delta\phi_j$ are neglected. Similarly, when the polarizer is oriented at 135°, the Jones vector after passage through it is given by

$$\frac{1}{4}\begin{pmatrix} -ir_2 - r_1 \\ ir_2 + r_1 \end{pmatrix}, \tag{A19}$$

and the output from the photodetector PD1 is in this case proportional to the quantity $I_{135^\circ} = (1/8)|-ir_2-r_1|^2$, where

$$I_{135^\circ} = (R/4)(1+\rho-\delta\phi). \tag{A20}$$

Equations (A18) and (A20) show that $\rho+\delta\phi$ and $\rho-\delta\phi$ can be obtained by separate measurements at different polarizer angles. If the polarizing beam splitter PBS2 is used instead of the polarizer, one can obtain $\rho+\delta\phi$ and $\rho-\delta\phi$ simultaneously at the two detectors. This allows the difference $\delta\phi$ to be monitored continuously at the output of the differential amplifier.

During the alignment process it is useful to monitor the outputs of the photodetector PD1 for the two different final polarizer angles in order to verify the interferometer operation. Another useful check is to rotate the quarter-wave plate QWP4. By using Eqs. (A13), (A14), and (A9), the transmitted light intensities in this case are proportional to the following quantities:

$$I_{45^\circ} = \frac{R}{4}(1+\sin^2 2\psi), \tag{A21}$$

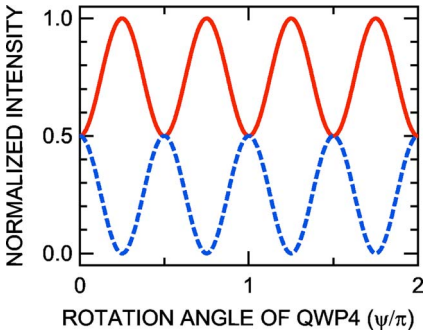

FIG. 11. (Color online) Plot of the simulated light intensity at the photodetectors as a function of the rotation angle of QWP4. The solid line corresponds to the light intensity for the polarizer set at 45° and the dashed line to that for 135°.

$$I_{135^\circ} = \frac{R}{4}\cos^2\psi, \tag{A22}$$

where ψ is the rotation angle of QWP4. The dependence of these two intensities on the rotation angle are shown in Fig. 11. The solid and dashed lines represent the normalized variations I_{45° and I_{135°, respectively. Possible set points for the interferometer correspond to the points where the two curves in Fig. 11 touch one another.

APPENDIX B: SHOT NOISE

The method for calculation of the shot noise relevant to the Sagnac interferometer is given in this appendix. The mean square noise current for an electron current is given by

$$\langle i_N^2\rangle = 2ei\Delta f, \tag{B1}$$

where e is the electronic charge, i is the photocurrent, and Δf is the detection bandwidth (see, for example, Refs. 59 and 60). But $i=Pe\eta/h\nu$ where P is the probe power incident on the detector and η is the external quantum efficiency of the detector (h is Planck's constant). Therefore, the rms noise current $\delta i=\langle i_N^2\rangle^{1/2}$ can be expressed as

$$\frac{\delta i}{i} = \sqrt{\frac{2h\nu\Delta f}{P\eta}} = \frac{\delta I}{I}, \tag{B2}$$

where I is the photodetector output voltage, proportional to the probe intensity. In the configuration of Fig. 1(c), extra noise is introduced when subtracting the voltages from the two photodetectors (without an increase in signal). This introduces an extra factor of $\sqrt{2}$,

$$\frac{\delta I}{I} = 2\sqrt{\frac{hc\Delta f}{P\lambda\eta}}, \tag{B3}$$

where λ is the probe wavelength and c is the velocity of light. In the present experiments, $\lambda=830$ nm. An estimate of the relative noise signal caused by the shot noise in our experiment can be obtained by setting $\eta=0.8$ for the photodiodes in question,

$$\frac{\delta I}{I}\sqrt{\frac{P}{\Delta f}} \approx 8\times 10^{-10}\sqrt{\mathrm{W/Hz}}. \tag{B4}$$

For the typical probe power $P=75$ μW (incident on each photodetector) combined with the detection bandwidth $\Delta f=300$ Hz, the predicted rms shot noise corresponds to $\sim 2\times 10^{-6}$ expressed as a relative intensity change. This is of the same order as the experimentally measured noise level.

We can express this noise level as a phase change as follows: if we detect, for example, a phase difference $\delta\phi$ related to I by $I=I_0+I_0\delta\phi$ (as in our interferometer when ρ is negligible), then $\delta I/I=(I-I_0)/I_0=\delta\phi$, where δI and $\delta\phi$ refer to a general change in these quantities. Neglecting photoelastic effects, the outward surface displacement is given by $\delta z=-\lambda\delta\phi/4\pi$, so the shot noise limit expressed as a rms displacement δz is given by

$$\delta z\sqrt{\frac{P}{\Delta f}} = \frac{1}{2\pi}\sqrt{\frac{h\lambda c}{\eta}}. \tag{B5}$$

Using the same parameters as above, we obtain

$$\delta z\sqrt{\frac{P}{\Delta f}} \approx 1\times 10^{-16}\ \mathrm{m}\sqrt{\mathrm{W/Hz}} = 1\times 10^{-4}\ \mathrm{pm}\sqrt{\mathrm{W/Hz}}. \tag{B6}$$

For our detection bandwidth and probe beam power at the photodetectors, the predicted rms shot noise corresponds to $\delta z\approx 0.2$ pm.

[1] J. P. Wolfe, *Imaging Phonons: Acoustic Wave Propagation in Solids* (Cambridge University Press, Cambridge, 1998).
[2] R. E. Vines, S.-I. Tamura, and J. P. Wolfe, Phys. Rev. Lett. **74**, 2729 (1995).
[3] R. E. Vines, M. R. Hauserand, and J. P. Wolfe, Z. Phys. B: Condens. Matter **98**, 255 (1995).
[4] Y. Sugawara, O. B. Wright, and O. Matsuda, Rev. Sci. Instrum. **74**, 519 (2003).
[5] Y. Sugawara, O. B. Wright, O. Matsuda, M. Takigahira, Y. Tanaka, S. Tamura, and V. E. Gusev, Phys. Rev. Lett. **88**, 185504 (2002).
[6] Y. Sugawara, O. B. Wright, and O. Matsuda, Appl. Phys. Lett. **83**, 1340 (2003).
[7] S. Shiokawa, M. Ueda, T. Moriizumi, T. Yasuda, and T. Sato, Jpn. J. Appl. Phys. **13**, 1907 (1974).
[8] K. Nakano, K. Hane, S. Okuma, and T. Eguchi, Opt. Rev. **4**, 265 (1997).
[9] Y. Zhou, T. W. Murray, and S. Krishnaswamy, IEEE Trans. Ultrason. Ferroelectr. Freq. Control **49**, 1118 (2002).
[10] J. L. Blackshire, S. Satihish, B. D. Duncan, and M. Millard, Opt. Lett. **27**, 1025 (2002).
[11] C. Trillo, D. Cernadas, A. F. Doval, C. López, B. V. Dorrío, and J. L. Frenández, Appl. Opt. **42**, 1228 (2003).
[12] K. L. Telschow, V. A. Deason, R. S. Schley, and S. M. Watson, J. Acoust. Soc. Am. **106**, 2578 (1999).
[13] R. Adler, A. Korpel, and P. Desmares, IEEE Trans. Sonics Ultrason. **SU-15**, 157 (1968).
[14] Y. Hong, S. D. Sharples, M. Clark, and M. G. Somekh, Appl. Phys. Lett. **83**, 3260 (2003).
[15] G. I. Stegeman, IEEE Trans. Sonics Ultrason. **SU-23**, 33 (1976).
[16] J. B. Gualtieri and J. A. Kosinski, IEEE Trans. Instrum. Meas. **45**, 872 (1996).
[17] J. V. Knuuttila, P. T. Tikka, and M. M. Salomaa, Opt. Lett. **25**, 613 (2000).
[18] A. Neubrand and P. Hess, Appl. Phys. Lett. **71**, 227 (1992).
[19] J. A. Rogers, A. A. Maznev, M. J. Banet, and K. A. Nelson, Annu. Rev. Mater. Sci. **30**, 117 (2000).
[20] A. G. Every, Meas. Sci. Technol. **13**, R21 (2002).
[21] C. Glorieux, J. D. Beers, E. H. Bentefour, K. V. de Rostyne, and K. A. Nelson, Rev. Sci. Instrum. **75**, 2906 (2004).
[22] S. G. Pierce, B. Culshaw, W. R. Philip, L. Lecuyer, and R. Farlow, Ultrasonics **35**, 105 (1997).
[23] J. R. Sandercock, Solid State Commun. **26**, 547 (1978).
[24] D. H. Hurley and O. B. Wright, Opt. Lett. **24**, 1305 (1999).
[25] B. Perrin, B. Bonello, J. C. Jeannet, and E. Romatet, Prog. Nat. Sci. **S6**, 444 (1996).
[26] W. M. Diffey and W. F. Beck, Rev. Sci. Instrum. **68**, 3296 (1997).
[27] J. Bowers, R. Jungerman, B. Khuri-Yakub, and G. Kino, J. Lightwave

Technol. **1**, 429 (1983).
[28] T. Jang, S. Lee, I. Kwon, W. Lee, and J. Lee, IEEE Trans. Ultrason. Ferroelectr. Freq. Control **49**, 767 (2002).
[29] P. A. Fomitchov, A. K. Kromine, S. Krishuaswamy, and J. D. Achenbach, IEEE Trans. Ultrason. Ferroelectr. Freq. Control **47**, 584 (2000).
[30] B. Mitra, A. Shelamoff, and D. J. Booth, Meas. Sci. Technol. **9**, 1432 (1998).
[31] J. J. Alcoz and H. F. Taylor, IEEE Trans. Ultrason. Ferroelectr. Freq. Control **37**, 302 (1990).
[32] D. H. Hurley and K. L. Telschow, Phys. Rev. B **71**, 241410 (2005).
[33] T. Guenther, V. Emilini, F. Intonti, C. Lienau, T. Elsaesser, R. Notzel, and K. H. Ploog, Appl. Phys. Lett. **75**, 3500 (1999).
[34] L. C. Downer, R. L. Fork, and C. V. Shank, J. Opt. Soc. Am. B **2**, 595 (1985).
[35] The noise reduction could be further improved by normalizing the ac voltage output of the photodetectors (detected by a lock-in amplifier) by their average dc voltage output. We found that the laser source we used was sufficiently stable to make this unnecessary.
[36] C. Thomsen, H. T. Grahn, H. J. Maris, and J. Tauc, Phys. Rev. B **34**, 4129 (1986).
[37] O. B. Wright and K. Kawashima, Phys. Rev. Lett. **69**, 1668 (1992).
[38] H. Yamazaki, O. Matsuda, O. B. Wright, and G. Amulele, Phys. Status Solidi C **1**, 2979 (2004).
[39] H. Yamazaki, O. Matsuda, and O. B. Wright, Phys. Status Solidi C **1**, 2991 (2004).
[40] The two probe pulses give opposite contributions to the output signal, but delayed in time by $\delta\tau$. See Ref. 41 for a more detailed explanation.
[41] Y. Sugawara, O. B. Wright, O. Matsuda, and V. E. Gusev, Ultrasonics **40**, 55 (2002).
[42] T. Saito, O. Matsuda, and O. B. Wright, Phys. Rev. B **67**, 205421 (2003).
[43] O. Matsuda, T. Tachizaki, T. Fukui, J. J. Baumberg, and O. B. Wright, Phys. Rev. B **71**, 115330 (2005).
[44] The insertion of Faraday rotators is discussed by O. B. Wright, D. H. Hurley, and O. Matsuda, in U.S. Patent Nos. 6549285, 6552799, and 6552800.
[45] W. S. Capinsky and H. J. Maris, Rev. Sci. Instrum. **67**, 2720 (2000).
[46] This frequency of ~300 Hz refers to the laboratory time scale, as opposed to the nanosecond time scale of the data itself.
[47] C. Scott, in *Introduction to Optics and Optical Imaging*, edited by R. F. Hoyt (Institute of Electrical and Electronics Engineers, Piscataway, NJ, 1988), p. 310.
[48] M. Kempe and W. Rudolph, Opt. Lett. **18**, 137 (1993).
[49] It is possible to choose different focal lengths for the two confocal lenses. This allows the sensitivity of the lateral scanning to mirror angle to be changed according to the ratio of the focal lengths.
[50] We assume that the axes of the Gaussian function are aligned with our coordinate axes x and y. The ellipticity arises from slight errors in optical alignment and the passage of the beams through the SHG crystal.
[51] J. P. Wolfe, Phys. Today **48**(9), 34 (1995).
[52] The pump spot size does not limit the spatial resolution for detection, but it does play a role in determining the frequency spectrum of the SAWs: the SAW pulse duration is typically somewhat greater than the SAW propagation time across the pump spot. This increase in duration is related to the thermal diffusion in the film and substrate.
[53] See EPAPS Document No. E-RSINAK-77-250604 for an animation corresponding to the data for the SAW propagation. This data can be reached through a direct link in the online article's HTML reference section or via the EPAPS homepage (http://www.aip.org/pubservs/epaps.html).
[54] C. Glorieux, K. Van de Rostyne, K. Nelson, W. Gao, W. Lauriks, and J. Thoen, J. Acoust. Soc. Am. **110**, 1299 (2001).
[55] C. Glorieux *et al.*, J. Acoust. Soc. Am. **74**, 465 (2003).
[56] F. Jenot, M. Ouaftouh, M. Duquennoy, and M. Ourak, J. Appl. Phys. **97**, 094905 (2005).
[57] B. L. Petersen, G. Meyer, T. Crecelius, and G. Kaindl, Appl. Phys. Lett. **73**, 538 (1998).
[58] B. E. A. Saleh and M. C. Teich, *Fundamentals of Photonics* (Wiley, New York, 1991).
[59] N. Gershenfeld, *The Physics of Information Theory* (Cambridge University Press, Cambridge, 2000).
[60] J. W. Wagner and J. Spicer, J. Opt. Soc. Am. B **4**, 1316 (1987).